Actual Out-of-Band Emissions from Massive MIMO Antennas

RIZK Christ⁽¹⁾, SEGUENOT Eric⁽¹⁾, KALTENBERGER Florian⁽²⁾, NUSSBAUM Dominique⁽¹⁾, MORO Andrea⁽³⁾, SINICCO Alessandro⁽³⁾, ARORA Sagar⁽⁴⁾

(1) INNOV/ANT Department, ORANGE, Sophia Antipolis, France
(2) Communication systems Department, Eurecom, Sophia Antipolis, France
(3) Andrew, Agrate Brianza, Italy
(4) OpenAirInterface, Sophia Antipolis, France

Abstract—In this paper, we address the issue of out-of-band (OOB) emissions in 5G Massive Multiple Input Multiple Output (MIMO) antennas. Due to the limited available spectrum, signals in different allocated bands are at risk of causing interference in adjacent frequency bands. The spatial behavior of OOB emissions depends on the operating regime of the power amplifiers (PAs). In the nonlinear regime, and in the absence of digital predistortion (DPD), the radiation is coherent across subarrays, causing the OOB emissions to be beamformed in the direction of the desired signal. Conversely, in the linear regime, with DPD applied, the radiation remains coherent for inband components, but the OOB emissions become decorrelated across subarrays, effectively turning the radiating elements into uncorrelated noise sources that radiate incoherently. We investigated this phenomenon experimentally in an anechoic chamber using a 32TX/32RX n78-band Massive MIMO antenna provided by Andrew-Amphenol. The results aligned well with theoretical expectations and confirmed the predicted benefits of spatial averaging, particularly its positive impact on the adjacent channel leakage ratio (ACLR), with radiated measurements showing better performance than conducted ones. This study highlights the spatial filtering advantages of Massive MIMO and supports its integration into standardization efforts and network planning.

Index Terms—5G, MIMO, OOB, Experimental platforms, OTA measurements.

I. INTRODUCTION

Massive MIMO technology is a cornerstone of current and next-generation wireless communication systems. By deploying large antenna arrays at base stations, Massive MIMO enables the spatial focus of energy, resulting in substantial improvements in spectral efficiency, system throughput, and interference suppression. These performance gains are achieved primarily through coherent beamforming techniques, which direct the desired signal energy to the intended users while minimizing leakage in other directions [1].

While the spatial behavior of in-band signals in Massive MIMO systems is well understood and extensively documented, the characteristics of OOB emissions arising from nonlinear hardware effects such as PA distortions remain less explored. Out-of-band emissions are unwanted signal components that fall outside the useful bandwidth of the frequency range used to carry actual data. These emissions don't contribute to communication and can interfere with nearby channels.

They are caused by hardware imperfections like amplifier non-linearities or poor filtering. To reduce them, systems use filters and signal processing to confine energy within the useful bandwidth and meet regulatory limits. Although these emissions are spectrally suppressed due to DPD and spectral cavity filtering, they can still pose significant challenges in meeting regulatory spectral masks and in minimizing adjacent channel interference.

Nonlinearities, particularly in power amplifiers, lead to spectral regrowth and intermodulation products that extend beyond the main signal band. Among these, third-order intermodulation distortion is particularly critical due to its proximity to the signal band and its relatively high power compared to higher-order components. Larsson and Van der Perre [2] theoretically demonstrated that nonlinear distortion is correlated to the useful signal (e.g., third-order components arising from the transmitted waveform itself), and when the PA operates in the nonlinear regime without DPD, these unwanted components can be beamformed similarly to the desired signal. As a result, distortion power in the main beam direction can scale coherently with the number of antennas, potentially causing OOB interference in critical directions.

In contrast, when PAs operate in the linear regime and DPD is applied, non-linear distortions are sufficiently surpressed such that the OOB emissions become decorrelated across antenna subarrays. In this case, while the useful signal components are coherently combined, the OOB emissions behave as low-power, uncorrelated noise sources, significantly reducing their impact on adjacent frequency bands [3].

In this paper, Section II presents a theoretical model of the problem, followed by the experimental setup used to perform the measurements, with a focus on the OOB components relative to the antenna array. Theoretical expectations are developed and subsequently validated through experimentation. Section III provides a detailed analysis of the measurement results. Finally, Section IV summarizes the key contributions and insights of the study.

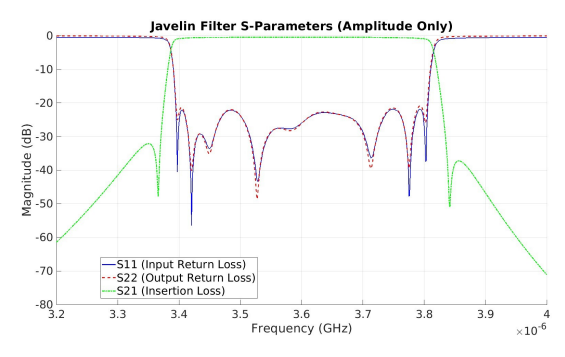


Fig. 1: Antenna internal cavity filter S-parameters.

II. THEORETICAL FRAMEWORK AND MEASUREMENT SETUP

A. Theoretical modeling

In this subsection, we will model the problem and the OOB emissions. We define OOB emissions as any unwanted emission immediately outside the channel used in the actual transmission band. The analysis is limited to the unwanted emissions within the [3.4–3.8]GHz band, as emissions outside this range are effectively suppressed by the cavity filter and therefore considered negligible as shown in Figure 1.

To support the preceding discussion, Figure 2 illustrates the fronthaul interface (FHI) between the ODU and ORU as described in II-D, followed by the RF transmission chains in the Spear Andrew antenna array. The TX block in the ADRV9029 contains the digital to analog and analog to digital conversions. A multitone OFDM baseband signal s(t) is fed into the RF transmission chain that modulates the baseband signal with the required carrier frequency ω_0 to a passband signal $s(t) = Re\left\{s(t)e^{i\omega_0t}\right\}$. The signal then passes through a power amplifier (PA) and is fed back to the DPD block. Let $y(t) = Re\left\{y(t)e^{i\omega_0t}\right\}$ denote the passband signal at the output of the PA, then the effect of the PA can be modeled in baseband by a third-order, memoryless Wiener Volterra model, nonlinear PA characterized by [4]:

$$y(\tilde{t}) = c_1 h(0) s(\tilde{t}) + c_3 h(0)^3 s(\tilde{t})^3,$$
 (1)

where h(0) is the complex Volterra Kernel and c_1 and c_3 are the 1^{st} and 3^{rd} order PA coefficients. The 2^{nd} order non linear intermodulations are suppressed by the cavity filter, therefore they are not taken into consideration.

Nonlinear power amplifiers are difficult to model accurately due to their inherent nonlinearities and the complex distortions they introduce, such as memory effects, thermal variations, and impedance mismatches, all of which add significant theoretical and practical modeling challenges, which is why we used the simplified theoretical model represented in equation (1) by fixing M=0 and for further simplification, we denote $k_1=c_1h(0)$ and $k_3=c_3h(0)^3$.

Additionally, each subarray output is affected by additive white Gaussian noise, denoted $w_m(t)$, which is assumed to be zero-mean with variance σ^2 and uncorrelated across subarrays.

The transmitted passband signal $y_m(t)$ from the m-th subarray can be approximated in baseband to:

$$\tilde{y_m(t)} = k_1 \tilde{s(t)} + k_3 \tilde{s(t)}^3 + w_m(t) \tag{2}$$

The signal $\tilde{y_m(t)}$ enters the beamforming block at the level of the radiating subarrays and will be phase shifted by $e^{j\phi_m}$ to produce:

$$y_{bm}(t) = \tilde{y_m(t)}e^{j\phi_m} \tag{3}$$

The Spear Andrew antenna array comprises of $M=16~\rm RF$ transmission chains as illustrated in Figure 2, all driven by the same passband signal s(t). In the far field, the signal and distortion components from each subarray combine coherently due to the constructive interference of the antenna array, while the noise terms sum incoherently. The total received signal is proportional to:

$$y(\tilde{t}) = \sum_{m=1}^{M} y_{bm}(\tilde{t}) = \sum_{m=1}^{M} y_{m}(\tilde{t}) e^{j\phi_{m}}$$

$$= \sum_{m=1}^{M} \left[k_{1}\tilde{s}(\tilde{t}) + k_{3}\tilde{s}(\tilde{t})^{3} + w_{m}(\tilde{t}) \right] e^{j\phi_{m}}$$

$$= k_{1}\tilde{s}(\tilde{t}) \sum_{m=1}^{M} e^{j\phi_{m}} + k_{3}\tilde{s}(\tilde{t})^{3} \sum_{m=1}^{M} e^{j\phi_{m}} + \sum_{m=1}^{M} w_{m}(\tilde{t})$$

Since the noise terms $w_m(t)$ are independent and identically distributed (i.i.d.), their sum is also Gaussian with zero mean and increased variance $M\sigma^2$. We denote this equivalent noise as:

$$w_{\text{eq}}(t) = \sum_{m=1}^{M} w_m(t) \sim \mathcal{N}(0, M\sigma^2)$$
 (5)

Since we are using the beam at boresight, the beamforming weights on all the subarrays are equal, thus the phases will be the same.

The complete expression for the far-field signal in the boresight direction is thus:

$$\tilde{y}(t) = Mk_1 \tilde{s}(t)e^{j\phi_m} + Mk_3 \tilde{s}(t)^3 e^{j\phi_m} + w_{eq}(t)$$
 (6)

We observe the decomposition into:

- Useful signal: $Mk_1s(t)e^{j\phi_m}$
- OOB emissions: $Mk_3\tilde{s(t)}^3e^{j\phi_m}$
- Noise: $w_{eq}(t)$

B. Closed loop DPD for digital MIMO transmitters

In this subsection, we describe the functionality and theoretical modeling of the digital predistortion (DPD) system implemented in the antenna array.

DPD is a critical technique for mitigating the nonlinear effects of PAs by pre-processing the transmit signals to cancel out amplifier-induced distortion.

The Volterra series offers a mathematical framework to describe nonlinear systems with memory. However, the full model is computationally expensive due to its exponential growth in parameters. Zhu and Brazil (2006) propose simplified forms such as memory polynomial models,

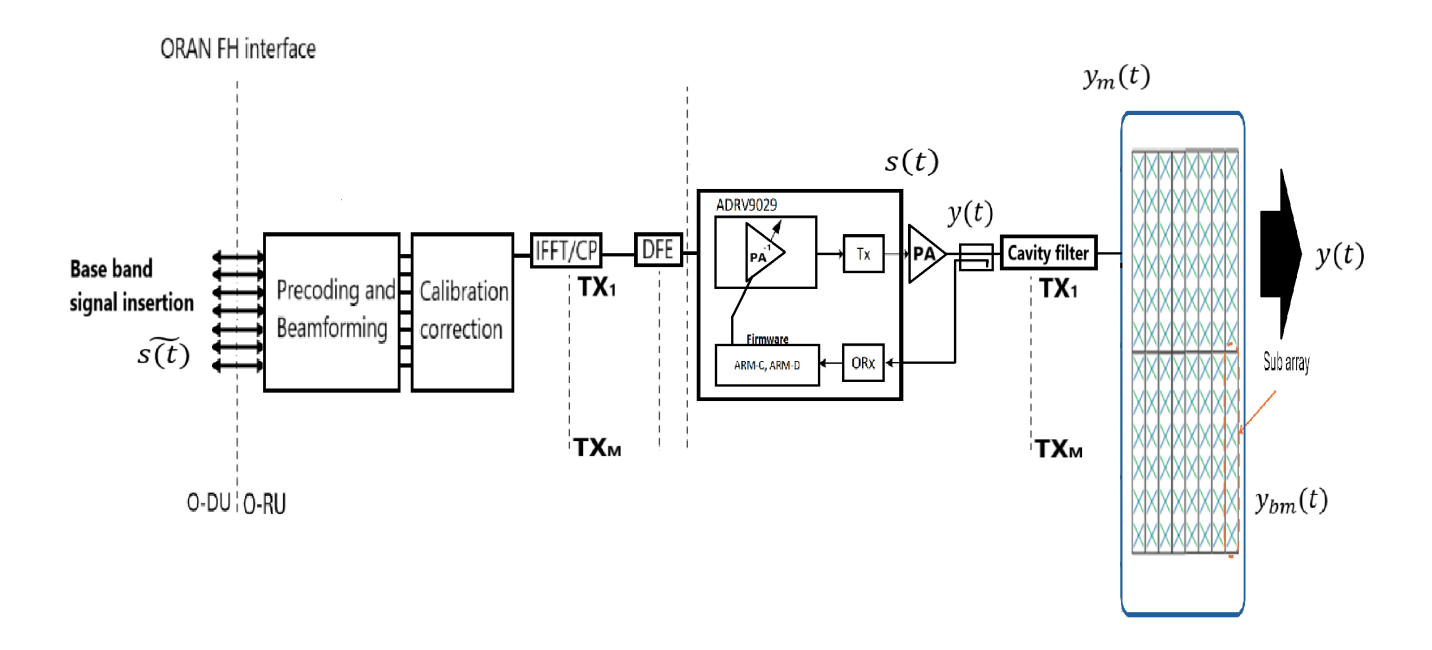


Fig. 2: RF Transmissions chain representation

Wiener/Hammerstein structures, and dynamic deviation methods. These allow efficient modeling while preserving accuracy, forming the theoretical basis for DPD algorithms [4].

Analog Devices' ADRV9025 transceiver applies a Generalized Memory Polynomial (GMP) model, a simplified Volterra form, for real-time DPD. It uses an observation receiver to capture the amplifier's output and an embedded processor to adapt DPD coefficients dynamically. The architecture prioritizes efficiency and robustness, implementing core ideas from Volterra theory in embedded hardware, it's a predecessor of the ADRV9029 transceiver [3].

The ADRV9025 system is a practical realization of the Volterra modeling principles. It adopts pruning techniques and efficient polynomial structures described in the academic literature to balance performance and computational cost. Thus, the theoretical framework supports the practical solution deployed in the device.

Since s(t) is a multitone OFDM signal, it contains multiple frequencies as subcarriers. The nonlinear operation $s(t)^3$ generates additional frequency components due to intermodulation [2]. Some of these intermodulation components are not filtered out by the cavity filter and can affect both the useful band and adjacent bands within the cavity filter bandwidth. The DPD's functionality is to linearize the non linear operation $k_3s(t)^3$ and reduce the important effect relative to the OOB emissions before reaching the beamforming block represented by $e^{j\phi_m}$ in equation (6).

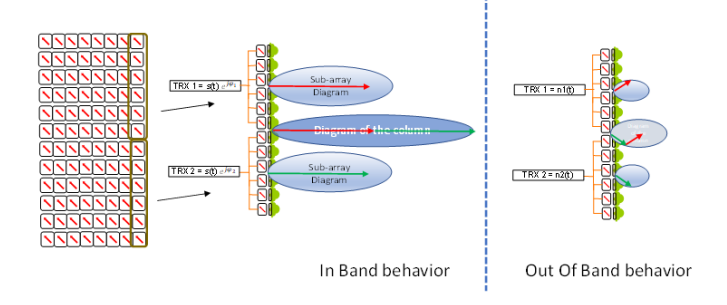


Fig. 3: Difference between In band and out of band spatial behavior

C. Spear Andrew antenna array modeling

We use the 3GPP model for antenna arrays as described in Section 5.2.3 of [5]. For the following argument, we will focus on only two vertically stacked subarrays, but later we will generalize to the whole antenna.

As illustrated in Figure 3, the transmitted signals from 2 vertical subarrays are expressed as:

$$\mathrm{TX}_1 = \tilde{s(t)}e^{j\phi_1}, \quad \mathrm{TX}_2 = \tilde{s(t)}e^{j\phi_2},$$

where $\tilde{s(t)}$ is the baseband signal injected into each subarray, and ϕ_1 and ϕ_2 are the phase shifts applied to each transceiver (TRX) chain, corresponding to a selected beamforming direction.

By adjusting the relative phase difference $\phi_2 - \phi_1$, the beam can be steered in the vertical plane. In the boresight

direction (i.e., the main beam axis), the phase shifts are equal, $\phi_1 = \phi_2$. In the linear operating regime of the PAs and with DPD activated, the radiation patterns of the subarrays add coherently.

Considering M subarrays, the resulting beam pattern is amplified by the array gain denoted M in the operating band.

In the OOB regions, these components are uncorrelated across subarrays and thus suppressed because of DPD, resulting only in having an array gain of M but no beamforming gain, and same thing goes for the noise components.

Equation (6) highlights two key effects when we add the beamforming gain to the desired signal alone:

- The desired signal scales coherently with DPD activated and PA in linear regime with a total gain of $20\log_{10}(M)=24$ dB. This 24 dB results from two contributions: a 12 dB beamforming gain (coherent combining) and a 12 dB power gain (from M antennas).
- The noise scales incoherently with an array gain of M of $10\log_{10}(M)=12$ dB. Emissions add incoherently across antennas. Hence, only the 12 dB power gain remains, while the 12 dB beamforming gain vanishes due to spatial averaging.

This behavior leads to a reduction in peak OOB radiation, an improvement in far-field adjacent channel leakage ratio (ACLR), and superior radiated ACLR performance compared to conducted measurements particularly in large antenna arrays.

D. Experimental setup

Spec	Comments	
Operating Band	3400-3800 MHz (Band n78)	
Standard	5G NR	
Number of TX/RX Paths	32	
Output Power	200 W	
Instantaneous/Occupied BW	200 MHz / 200 MHz (HW ready, SW	
	supports $1 \times 100 \text{ MHz}$)	
Number of Carriers	2 × 100 MHz (HW supports multiple	
	bandwidths: 20-100 MHz; SW	
	supports 1×100 MHz only)	
Number of Layers	16 DL, 8 UL	
Supported SCS	30 kHz and 60 kHz (SW supports only	
	30 kHz currently)	
Front Haul Interface	2 × 25Gb (SFP28, ORAN Cat B, SW	
	supports 1×25 Gb only)	
Total EIRP	77 dBm (2 × 74 dBm)	
Rx Sensitivity (100 MHz)	-89 dBm (1 Rx path); EIS: -114	
•	dBm/100 MHz	
Number of Antenna Elements	192 (12×8×2 configuration with 6×1	
	sub-arrays)	
Polarization mode	-45°, +45°	
Maximum Antenna Gain	24.3 dBi	
Dynamic Horizontal Steering	±48°	
Vert. Digital Steering Range	±3° (@6dB sidelobe suppression,	
	±1.5° @10dB sidelobe)	
Total Vertical Steering	-15° to +3° (includes -12° up via RET	
	motors and mechanical phase shifters)	
Power Consumption (W)	750 W (typical: 80% DL, 20% UL	
-	TDD ratio)	
Temperature Range	-40° to +55°	
Dimensions	730 × 430 × 150 mm; Volume 47L;	
	Weight 30 kg (*23 kg with bonded fin	
	heatsink)	

TABLE I: Spear Andrew antenna array specification table

Table I presents the primary RF characteristics of the Spear antenna array from Andrew-Amphenol. The term 32TX/32RX

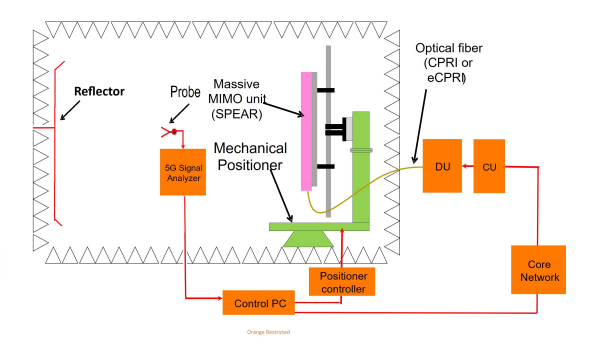


Fig. 4: OTA measurement setup

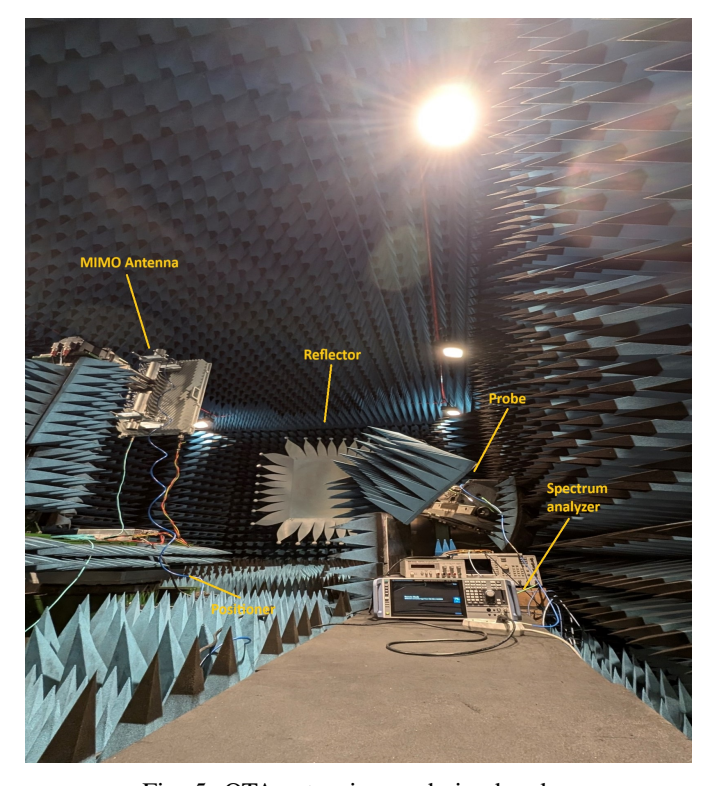


Fig. 5: OTA setup in anechoic chamber

indicates the presence of 32 transmit (TX) and 32 receive (RX) radio frequency chains. The antenna array has 192 radiating elements, grouped into 8 columns, 12 rows, and 2 polarizations. Each RF chain drives a subarray composed of 6 horizontally stacked single polarized radiating elements.

In our experiments, we utilized only the -45° polarization. Therefore, the effective number of subarrays is M=16.

Figure 4 illustrates the setup used for the Over the air (OTA) measurements. The MIMO antenna is mounted on a positioner that rotates in the azimuth plane to facilitate the measurement of radiation beam patterns. In our experiments, we plotted the radiation patterns in the elevation plane, with $\theta \in [-60^\circ, 60^\circ]$, by rotating the antenna array to 90° relatively to the positioner. The beam is emitted toward a reflector, which redirects the signal toward the measurement probe. The signal then passes

through the probe to a spectrum analyzer for visualization and analysis of the beam pattern.

The Spear Andrew radio unit (RU) is compliant to the O-RAN 7.2 fronthaul specifications. To stimulate the RU we use the OpenAirInterface (OAI) distributed unit (DU) [6] in the so-called phy-test mode, which uses a simplified scheduler that schedules physical downlink control channels (PDSCH) with random data and parameters given in Table II¹. In our setup the O-RAN C-plane is deactivated in the RU (i.e., the RU ignores the C-plane messages from the DU) and the beam ID is controlled from the RU config file.

The RU and the DU are both connected to a Fibrolan Falcon RX/G fronthaul switch, which acts as a grandmaster for the precision time synchronization (PTP) protocol. A detailed tutorial of the setup can be found in [7].

phy-test options	Value
Downlink PRBs (-M)	273
Uplink PRBs (-T)	273
Number UL layers (_l)	1
Number DL layers (-L)	1
Downlink slots configuration (-D)	524287
Uplink slots configuration (-U)	0
DL MCS (-m)	0 (QPSK)
UL MCS (-t)	0 (QPSK)

Config File	Value
TDD periodicity	10 ms
TDD configuration pattern	19D1S
Subcarrier spacing	30kHz

TABLE II: PHY Test and gNB Configuration

The transmitted waveform is a 5G NR-compliant OFDM signal with a 100 MHz bandwidth centered at 3.75 GHz. Measurements were taken across the 3.3–3.9 GHz range to capture both in-band and OOB emissions. The Andrew-Amphenol antenna array supports fixed Beam ID beamforming. Fixed Beam ID beamforming uses a set of precomputed weights, each associated with a unique Beam ID, to steer beams in specific directions. The weights are stored in a lookup table and loaded into the radiating elements via the beamforming network when a Beam ID is selected, enabling fast and efficient beam switching. The beam at boresight with highest directivity from the antenna array's codebook was used in the experiments, defined by $(\phi = 0^{\circ}, \theta = -6^{\circ})$, which corresponds to the boresight beam and provides maximum directivity. We acknowledge that the current analysis focuses on boresight beamforming. For off-boresight beams, mutual coupling and array calibration imperfections may modify the OOB radiation characteristics, potentially reducing the

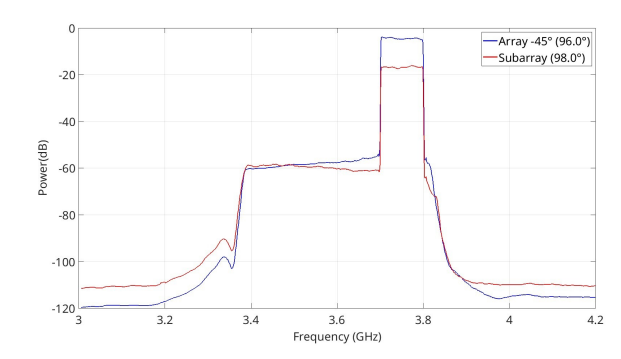


Fig. 6: Full antenna array spectrum compared to one subarray spectrum at bore sight with DPD in isopower mode

coherence of distortion products. A detailed study of these effects is left for future work. Figure 5 shows a photograph of the experimental setup, corresponding to the schematic in Figure 4.

III. EXPERIMENTAL RESULTS

A. Maximum radiation comparison

Figure 6 illustrates the spectrum of the full antenna array at bore sight in isopower mode, where we only wish to study the beamforming gain in the full spectrum. We realize that within the main signal band channel, the power of the full antenna array is around 12 dB higher than a single subarray. This difference between the 2 band shapes indicates accurate phase alignment across the array and confirms the effectiveness of DPD in maintaining linearity within the PA's operating range.

At the band edges, however, the full coherent array exhibits almost equal behavior in the spectrum variations. This result highlights the dual effect of spatial filtering and DPD in suppressing OOB emissions when the PAs operate in their linear region.

These findings demonstrate that Massive MIMO architectures offer substantial improvements in radiated adjacent channel leakage ratio (ACLR). By exploiting array scaling and the uncorrelated nature of residual distortion, radiated ACLR performance can be enhanced by up to 12 dB, thereby enabling compliance with stringent emission standards such as the 3GPP 45 dBc requirement [8].

Disabling the DPD function results in the emergence of nonlinear distortion components through operating the PAs in the non linear regime, primarily the third and fifth order harmonics (denoted as H3 and H5), which leak from the main signal band into adjacent frequency bands. As illustrated in Figure 7, although a portion of these harmonics remains confined within the cavity filter's passband (3.4–3.8 GHz), they generate prominent spectral shoulders that degrade inband signal quality and increase adjacent channel interference in the left part of the useful band, while the harmonics in the right side are suppressed by the cavity filter.

¹The parameters -D and -U are a bitmaps, where each bit corresponds to a slot. The number 524287 corresponds to all 19 DL slots being fully loaded.

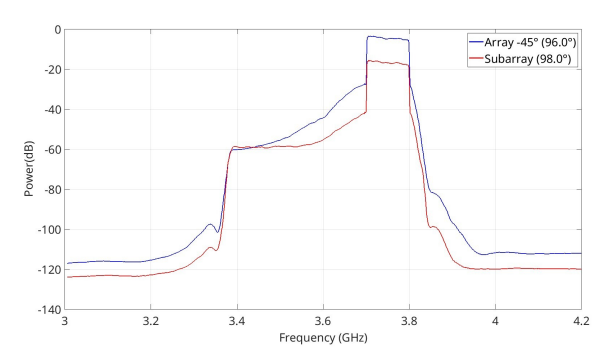


Fig. 7: Full antenna array spectrum compared to one subarray spectrum at bore sight without DPD in isopower mode

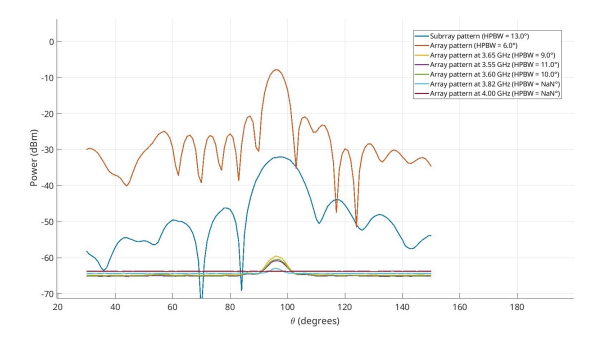


Fig. 8: Comparison of various array radiation patterns at different frequencies in OOB to the measured subarray and array pattern with DPD.

B. Coherent radiation in PA linear regime

The goal of this analysis is to compare the measured radiation patterns of a single subarray and the full beamformed antenna array. The comparison focuses on angles within the elevation plane range of $-60^{\circ} \leq \theta \leq 60^{\circ}$. In what follows, we adopt the elevation convention defined by the 3GPP specifications [5] where the elevation plane's reference is the vertical axis of the antenna array, so the spatial elevation angles are shifted to 90° . This evaluation aims to assess alignment with theoretical expectations, validate the accuracy of beam steering and implementation consistency, and quantify deviations in main lobe direction and side lobe levels.

1) In band behaviour: With the implementation of the full array, the beam gain increased by 24 dB, as shown in Figure 8, indicating a significant improvement in directive performance. This gain enhancement is primarily attributed to the constructive interference of signals from multiple array elements, which boosts the radiated power in the desired direction when the PAs operate in the linear regime and DPD is enabled.

In addition to the gain improvement, the number and levels of side lobes were notably reduced. This contributes to better suppression of unwanted radiation in off-axis directions, thereby improving overall beam efficiency and reducing potential interference.

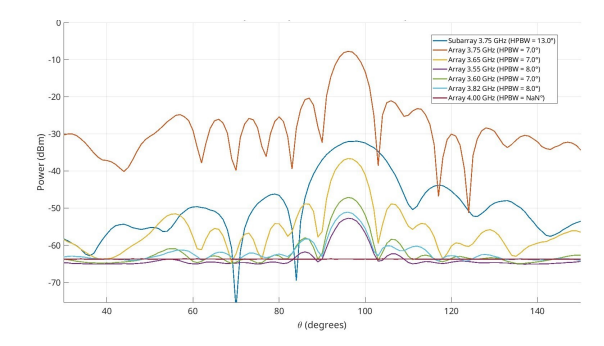


Fig. 9: Comparison of various array radiation patterns at different frequencies in OOB to the measured subarray and array pattern without DPD.

2) OOB behaviour: The OOB radiation pattern of the full antenna array at the different OOB frequencies closely resembles that of a single subarray, as shown in the different curves in Figure 8, as expected and by comparing the Half Power Beamwidth (HPBW) that are close to the one of the measured subarray. This observation indicates a lack of spatial coherence in the OOB emissions.

Unlike in-band signals, which are coherently combined across the array to form a directive beam, the OOB components do not benefit from such constructive spatial alignment. As a result, the full array behaves more like a collection of independent radiators rather than a coherent beamforming system in the OOB region.

This characteristic explains the inherent suppression of OOB emissions commonly observed in massive MIMO systems. Since the OOB signals from different antenna elements do not add coherently, their combined radiation averages out spatially, reducing the overall OOB power projected in any specific direction.

C. Coherent radiation in PA non linear regime

At elevated transmit power levels and without DPD, the PAs in the array enter their nonlinear operating region, giving rise to intermodulation distortion products. Specifically, third-order H3 and fifth-order H5 components were observed to emerge prominently in the measured spectra. These distortion components are not random or spatially diffuse; rather, they exhibit clear signs of spatial coherence.

Spectral measurements in Figure 9 show that the intermodulation products are beamformed in the same direction as the in-band signal. Specifically, the OOB radiation pattern of the full array at different frequencies closely follows the main array pattern, with HPBW similar to the one at 3.75 GHz. This confirms that the distortion products from each element combine coherently and are directed along the same spatial beam as the desired signal.

IV. CONCLUSIONS

This study provided a comprehensive experimental and theoretical investigation into the spatial characteristics of out-of-band (OOB) emissions in massive MIMO systems.

Using a commercial-grade 32TX/32RX 5G antenna array, we demonstrated how the coherence properties of both inband and OOB emissions depend heavily on the power amplifier's (PA's) operating regime and the application of digital predistortion (DPD). In the linear regime with DPD enabled, OOB components across subarrays are decorrelated, resulting in incoherent radiation and improved adjacent channel leakage ratio (ACLR). Conversely, in the nonlinear regime without DPD, OOB emissions become spatially coherent and are beamformed in the same direction as the desired signal, leading to an increased risk of interference.

These findings support the inclusion of spatial OOB behavior in future standardization efforts and network planning methodologies. We conclude that the study by Larsson and Van der Perre is valid only when DPD is deactivated and the PAs operate in the non linear regime [1].

While this study focused on the n78 band (3.4–3.8 GHz), the observed spatial characteristics of OOB emissions are fundamentally governed by array configuration, PA nonlinearity, and signal correlation factors that remain relevant across frequency bands. Consequently, the results can be generalized to higher frequency ranges, including anticipated 6G bands since Larsson and Van der Perre's study is carried out for any Signals with a general, but band-limited, spectrum that will see a widening of their bandwidth. In such bands, OOB emissions

may become even more critical due to denser arrays, wider bandwidths, and more pronounced hardware nonlinearities.

REFERENCES

- E. G. Larsson, O. Edfors, F. Tufvesson, and T. L. Marzetta, "Massive mimo for next generation wireless systems," *IEEE communications* magazine, vol. 52, no. 2, pp. 186–195, 2014.
- [2] E. G. Larsson and L. Van Der Perre, "Out-of-band radiation from antenna arrays clarified," *IEEE Wireless Communications Letters*, vol. 7, no. 4, pp. 610–613, 2018.
- [3] "ADRV9029 DPD System Overview," https://wiki.analog.com/resources/ eval/user-guides/adrv9029/dpd_system_overview2, Mar. 2021, analog Devices Wiki. Last modified 28 Mar 2021 by Anand Kumar.
- [4] A. Zhu and T. J. Brazil, "An overview of volterra series based behavioral modeling of rf/microwave power amplifiers," in 2006 IEEE annual wireless and microwave technology conference. IEEE, 2006, pp. 1–
- [5] 3GPP, "Study on new radio access technology: Radio Frequency (RF) and co-existence aspects (Release 14)," 3rd Generation Partnership Project (3GPP), Tech. Rep. TR 38.803 V14.4.0, June 2024, 3GPP Technical Report. [Online]. Available: https://www.3gpp.org/ftp/Specs/archive/38_series/38.803/38803-d40.zip
- [6] F. Kaltenberger, T. Melodia, I. Ghauri, M. Polese, R. Knopp, T. T. Nguyen, S. Velumani, D. Villa, L. Bonati, R. Schmidt, S. Arora, M. Irazabal, and N. Nikaein, "Driving innovation in 6g wireless technologies: The openairinterface approach," *Computer Networks*, vol. 269, no. 111410, Sep. 2025.
- [7] T. Vladic et al., "ORAN_FHI7.2_Tutorial," EURECOM GitLab repository, develop branch, Apr. 2025, retrieved June 19, 2025.
- [8] 3GPP, "Base station (bs) radio transmission and reception (release 17)," 3rd Generation Partnership Project, Tech. Rep. TS 38.104, Mar. 2023.